Pair Plasma Instability in Homogeneous Magnetic Guide Fields

M.J. Pueschel[1,2,3,4a], R.D. Sydora[5], P.W. Terry[4],

B. Tyburska-Pueschel[1,4], M. Francisquez[6], F. Jenko[7], and B. Zhu[8]

[1]*Dutch Institute for Fundamental Energy Research,*

5612 AJ Eindhoven, The Netherlands

[2]*Eindhoven University of Technology,*

5600 MB Eindhoven, The Netherlands

[3]*Institute for Fusion Studies, University of Texas at Austin, Austin, TX 78712, USA*

[4]*University of Wisconsin-Madison, Madison, Wisconsin 53706, USA*

[5]*University of Alberta, Edmonton T6G 2E1, Canada*

[6]*MIT Plasma Science and Fusion Center,*

Cambridge, Massachusetts 02139, USA

[7]*Max-Planck-Institut für Plasmaphysik, 85748 Garching, Germany*

[8]*Lawrence Livermore National Laboratory, Livermore, California 94550, USA*

---

[a] corresponding author, `mj.p@utexas.edu`

Abstract

Pair plasmas, collections of both matter and antimatter particles of equal mass, represent a paradigm for the study of basic plasma science, and many open questions exist regarding these unique systems. They are found in many astrophysical settings, such as gamma-ray bursts, and have recently also been produced in carefully designed laboratory experiments. A central research in plasma physics is instability; however, unlike their more common ion-electron siblings, pair plasmas are generally thought to be stable to cross-field pressure gradients in homogeneous magnetic fields. It is shown here by means of kinetic full-f simulations that, when a pressure gradient is first established, the Gradient-driven Drift Coupling mode is destabilized and becomes turbulent. Force balance is eventually achieved by a combination of flattened pressure profile due to turbulent transport and establishment of a magnetic field gradient, saturating the growth. During the unstable phase, key physics can be captured by a δf gyrokinetic description, where it is shown analytically and numerically that parallel particle motion results in a coupling of all electromagnetic field components. A fluid model derived therefrom accurately predicts linear eigenmodes and is used to resolve global profile effects. For laser-based electron-positron plasma experiments, prompt instability is predicted with growth times much shorter than plasma lifetimes. Similarly, growth rates are calculated for the planned APEX experiment as well as gamma-ray burst scenarios, suggesting that the instability may contribute to the early evolution of these systems.

I. BACKGROUND

Most of the visible universe exists in a plasma state, where matter is ionized and can self-interact via electric and magnetic fields. Such interaction can take the form of waves [1] or instabilities [2, 3]; the latter arise from the growth of perturbations, which eventually saturate either due to a depleted energy source or due to nonlinear energy transfer, potentially leading to turbulence [4]. A large variety of plasma instabilities exists in disparate systems, both astrophysical and in the laboratory, and the drive physics can rely on pressure [5, 6], current [7], or velocity-space inhomogeneities [8, 9].

A special class of plasmas are those comprised simultaneously of matter and antimatter particles. In nature, electron-positron pair plasmas tend to be produced during highly energetic events, such as gamma-ray bursts (GRBs) [10]. In laboratory experiments, antiprotons have been studied intensively [11], but not at densities sufficient to produce a pair plasma, whereas collective effects and plasma behavior in electron-positron systems is an active topic of research. There, advances in laser-induced plasmas have been utilized [12–15]; a key consideration is the propensity for collective effects [16] and especially instability, such as the Weibel instability [9]. The latter is believed to be widely occurring, but requires opposing streams of plasma.

A Maxwellian pair plasma is not usually considered to be unstable. A preparatory theoretical study [17, 18] in the context of the planned APEX magnetic confinement device [19, 20] seems to confirm this expectation. It demonstrates that no instability occurs in a homogeneous guide field in the presence of density or temperature gradients when only electrostatic Φ and shear-magnetic $A_\parallel$ fluctuations are considered, i.e., compressional magnetic fluctuations $B_\parallel$ are ignored. Instability may be obtained by introducing guide field curvature [21], which will be present in APEX. Similarly, Ref. [22] considers instability of axisymmetrically confined pair plasmas.

When including $B_\parallel$ fluctuations in the analysis, new physics can enter the fray. In particular, the Gradient-driven Drift Coupling (GDC) instability [24], which was first seen in studies of magnetic reconnection [23], is driven by density or temperature gradients $\omega_n \equiv L_z/L_n$ or $\omega_T \equiv L_z/L_T$, respectively, and couples the $\mathbf{E} \times \mathbf{B}$ drift with the $\nabla B_\parallel$ drift to produce both a stable and an unstable mode branch. Here, L_z denotes the macroscopic normalization length scale and L_n (L_T) the background density (temperature) scale length. In addition

to driving instability and turbulence, GDC activity was observed to enhance reconnection rates.

The physical mechanism of the GDC can be described as follows. Consider a magnetized plasma – pair or ion-electron – immersed in a magnetic guide field B_0 along z and a density/temperature gradient along x. If a perturbation of the electrostatic potential Φ forms along the third direction at a wavenumber k_y, it produces an $\mathbf{E} \times \mathbf{B}$ drift along x that advects plasma from regions of lower and higher density/temperature. This results in a density/temperature perturbation at k_y, which corresponds to a compressional perturbation $B_\parallel$. As a consequence, a $\nabla B_\parallel \times \mathbf{B}$ drift arises, separating charges and reinforcing the original Φ perturbation, thus producing instability. The interplay between the two drifts gives rise to term *drift coupling*.

Irrespective of whether ion-electron or pair plasmas are considered, this mechanism works even at very low normalized electron pressure $\beta \equiv 8\pi n_{e0} T_{e0}/B_0^2 \ll 1$ for scenarios with little or no background magnetic shear; here, n_{e0} and T_{e0} denote the background electron density and temperature, respectively. B_0 is assumed to be homogeneous unless stated otherwise. Note that this implies that the equilibrium is, generally, not force-free, as density and temperature gradients are not offset by a variation of B_0. It is to be stressed that in an exactly force-balanced equilibrium, where the guide field scale length L_B balances the pressure gradient scale length L_p per $1/L_B = -(\beta/2)/L_p$, the GDC mode becomes marginal [28]. However, as will be shown here, the process by which a system achieves force balance can entail GDC excitation and saturation in a turbulent state that persists for a significant period of time.

In the context of magnetic reconnection turbulence in the solar corona [25], GDC activity may boost volumetric heating rates [24]. Another application arises in experiments at the Large Plasma Device, where discharges with $L_z = 17\,\mathrm{m}$, substantial $\beta \sim \mathcal{O}(0.01)$, and large pressure gradients $\omega_n \sim \omega_T \sim \mathcal{O}(100)$, exhibit fluctuation characteristics consistent with turbulence driven primarily by the GDC [26].

The remainder of this paper is structured as follows. In order to determine whether the assumptions (gyrokinetic approximation and δf with an equilibrium not in force balance) made in previous work [24] introduce artificial features, full-f fully kinetic simulations of an electron-positron system are described in Sec. II. In that setup, GDC instability and turbulence are observed before a combination of turbulent flattening of the driving gradient

4

and establishment of a magnetic field gradient lead to a disabling of the GDC drive. Building thereupon, a solution of the GDC dispersion relation for a simple and mathematically transparent electron-positron plasma system is derived analytically in Sec. III, elucidating the impact of parallel particle motion; the result is shown to agree with gyrokinetic simulations. A simple fluid model is obtained in Sec. IV, which recovers linear gyrokinetic results. Finally, Sec. V describes a number of physical systems and how GDC activity may impact observables therein: a laser-induced, a magnetically confined, and a GRB electron-positron plasma.

II.   KINETIC FULL-f SYSTEM

The Vlasov-Maxwell system of equations is solved for the full distribution function for a collisionless electron-positron plasma immersed at time $t = 0$ in a homogeneous guide field B_0, with a density profile as given in Fig. 1 and constant temperature throughout the domain; $\beta = 0.1$ and a Debye length of $\lambda_{\mathrm{D}} = 0.3$ normalized to the gyroradius ρ are chosen. Variation in the direction z along B_0 is not resolved. This is justified *a posteriori* by demonstrating in Sec. III that the $k_z = 0$ mode dominates; note, however, that in theory one may envision the nonlinear coupling of different k_z modes, which may complicate this situation. Such a scenario describes situations where a plasma of finite volume is quickly injected into a magnetic field, a situation of relevance to both natural and laboratory plasma systems.

These kinetic simulations for the full distribution function were carried out using a fully electromagnetic particle-in-cell simulation model in a slab geometry [27]. The (x, y, v_x, v_y, v_z) phase space is initialized with a density profile nonuniform along x and uniform along y, whereas a uniform temperature is assumed throughout the domain. A spectral method is used for solving Maxwell's equations, which allows for Fourier mode selection in the periodic y coordinate. The domain size in the x-y direction is taken to be 128×64 cells, and 20480 particles per cell were used.

Note that no physical meaning is assigned here to the amplitude, structure, and phases of the initial condition; the same applies to all simulations throughout this paper. Thus, the time that initially passes before the instability fully develops is of no relevance to the results reported here.
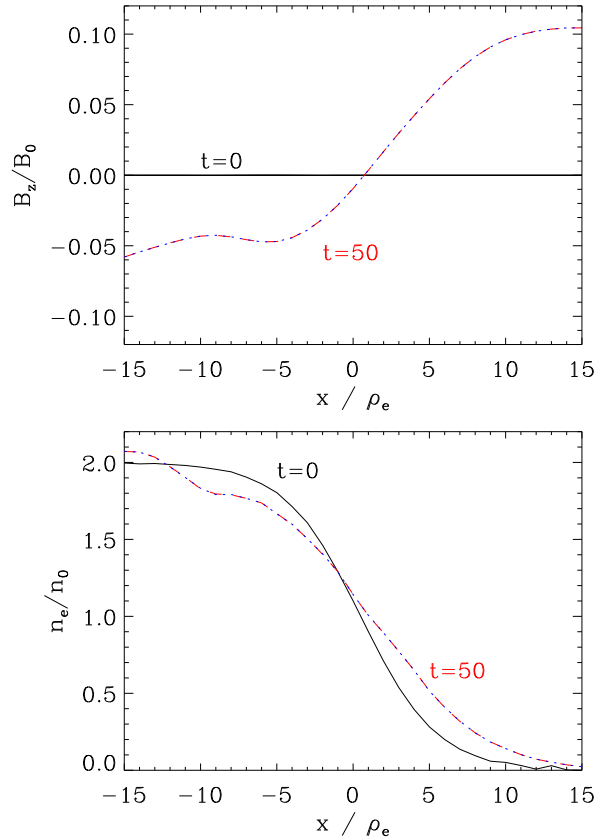
FIG. 1. Profiles of the parallel magnetic fluctuation (upper), i.e., excluding the homogeneous guide field $B_0 = 1$, and the electron density (lower). Black lines correspond to the initial profiles, while red and blue lines are data at time $t = 50$ of the base simulation and one with $A_\parallel$ artificially removed, respectively. Quasilinear flattening of the driving density gradient is observed, and the system is near force balance at $t = 50$.

As the system evolves, instability can clearly be seen in Fig. 2 (black lines), where amplitudes grow by more than one order of magnitude during the initial phase of the simulation. In the logarithmic panel, a second, separate simulation with only one finite k_y mode is included for comparison as a red dotted line, allowing for a somewhat cleaner estimate of the linear growth rate. In units of the thermal velocity $v_{\rm th} = (T_{\rm e0}/m)$, with mass m, divided by L_n, the growth rate thus reads $2\gamma \approx 0.13$; by comparison, the prediction from gyrokinetic theory and the fluid model detailed in Sec. IV (approximately matching the density gradient profile width) lie around $2\gamma \approx 0.40$. Throughout the linear growth phase, which stretches over only one order of magnitude due to computational expense, noise from the initial condition as well as quasilinear flattening pollute the result; the former is due to the eigenmode
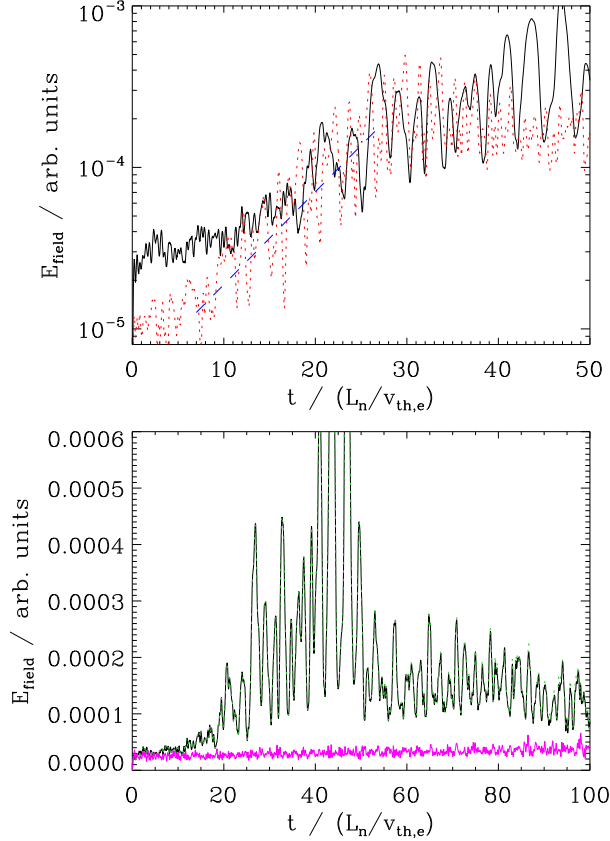
6

FIG. 2. Logarithmic (upper) and linear (lower) plots of the field energy in full-f kinetic simulations, showing linear growth and saturation (black lines). In the upper panel, a red dotted line shows growth in a separate simulation that includes only one finite k_y, corresponding to the fastest-growing wavenumber; a dashed blue line marks a fit to obtain the corresponding growth rate, as discussed in the text. The dotted green line in the lower panel refers to a simulation with $A_\parallel$ suppressed, while the solid pink line instead removes $B_\parallel$ at runtime. Growth and saturation thereof only occur in the former case.

not having fully converged in time, the latter refers to a self-consistent lowering of the density gradient as fluctuation levels grow—both can be expected to cause a reduction in the apparent growth rate. Considering these factors, growth is therefore roughly consistent in magnitude with the instability being of GDC type. This is further supported by the fact that no drift along y is observed in the simulation, conforming with the GDC property of zero or small frequencies $\omega \ll \gamma$.

These findings in isolation are merely suggestive; however, a variety of other properties point towards GDC as the underlying mechanism. As the GDC – for its $k_z = 0$ mode

7

branch – relies solely on the interplay of Φ and $B_\parallel$ fluctuations, tests can be designed that help determine the nature of the instability at hand. Shown as a dark yellow dotted line in the linear (lower) panel of Fig. 2 (almost exactly overlying the back line) is a separate simulation where perpendicular magnetic fluctuations $A_\parallel$ were artificially removed, clearly demonstrating insensitivity to this change; conversely, another simulation, shown in the same figure as a pink line, was performed with self-consistent $A_\parallel$ but artificially suppressed $B_\parallel$, leading to no instability or turbulence. These findings are again consistent with GDC properties, as is the fact that the growth rate scales with β, as confirmed by a separate simulation at $\beta = 0.05$.

In Fig. 1, red and blue lines correspond to profiles of $B_\parallel$ (not including the background field $B_0 = 1$) and the total density for the full and the $A_\parallel$-suppressed simulation, respectively, at a moment in time when growth of the fluctuations has ended. Again, no difference is observed when removing $A_\parallel$. Furthermore, the new field gradient and flattened density gradient, respectively $\omega_n = L_z/L_n \approx 0.12$ and $\omega_B = L_z/L_B \approx -0.0097$ when fitted in the range $-5 \le x \le 5$, are within 20% of being force-balanced for the present value of $\beta = 0.1$, as that condition reads $-\beta\omega_n = \omega_B$ [28].

As an aside, regarding the situation in the Large Plasma Device, where simulations in non-balanced equilibria capture experimental trends in helium plasmas, two possible explanations could be investigated. First, a small radial mismatch between the magnetic field and steep-density-gradient regions can lead to a significant deviation from force balance. Second, at plasma injection, a density gradient exists, but there is no initial field gradient; the fluctuation characteristics on which the validation study in Ref. [26] focuses may well be created during the saturation onset or persist for significant periods past that point, as the data in Fig. 2 at $t > 40$ suggests.

Quasilinear flattening of the density profile, in combination with the quasilinear establishment of a magnetic-field gradient causes the turbulent drive to turn off; this, however, does not preclude other saturation physics from being at play [26]. In particular, the existence of a mirror GDC, or a pseudo-eigenmode [29] variant thereof, would allow energy transfer to stable eigenmodes to contribute to saturation under the right conditions [30], a possibility that may be investigated further in the future.

These full-f kinetic simulations have demonstrated that a pair-plasma system initially not in force balance will evolve by exciting GDC instability, whose turbulent transport then

adjusts the pressure and magnetic field profiles until the system is force-balanced and linearly stable. In light of this finding, the focus is now shifted to the pre-equilibration phase, where the δf approximation is valid.

III.   GYROKINETIC TREATMENT AND PARALLEL DYNAMICS

Strong magnetization separates the cyclotron motion from GDC time scales, which for electron-positron plasmas are on the order of the transit time L_z/v_{te}, where $v_{\text{te}} \equiv v_{\text{th}}$ is the electron thermal velocity. Using the gyrokinetic approximation [31], one may then eliminate the Larmor time scale and effectively reduce orbital particle motion to a ring with distributed charge density. The normalized equations for the implementation used here are described in Ref. [23], to which the reader is referred for further detail. For the purpose of studying electron-positron plasmas, a number of simplifications may be introduced: The electron and positron species, respectively denoted by e and p, have identical mass m and background density but can also be assumed to have identical background temperatures due to the pair creation process as well as an efficient equilibration process. One may thus set $m_{\text{e}} = m_{\text{p}} = n_{\text{e}0} = n_{\text{p}0} = T_{\text{e}0} = T_{\text{p}0} = v_{\text{te}} = v_{\text{tp}} = 1$. Furthermore, identical gyroradii $\rho_{\text{e}} = \rho_{\text{p}} = 1$, normalized gradients $\omega_{T\text{e}} = \omega_{T\text{p}} = \omega_T = L_z/L_T$ and $\omega_{n\text{e}} = \omega_{n\text{p}} = \omega_n = L_z/L_n$, and background distribution functions $F_{0\text{e}} = F_{0\text{p}} = \pi^{-3/2} \exp(-v_{\parallel}^2 - \mu B_0)$ are implied, where $v_{\parallel}$ and μ are the velocity coordinate along z and the magnetic moment, respectively. Lastly, the electric charges are $q_{\text{p}} = 1 = -q_{\text{e}}$. Note that simply using a different mass unit makes all subsequent results directly applicable to any other pair plasma, such as proton-antiproton.

In a homogeneous magnetic field, one may set $B_0 = 1$ throughout the periodic domain. Linear modes in a collisionless electron-positron plasma are then described by the Vlasov equation for species j

$$i\omega_{\text{c}} g_j = -\left[\omega_n + \left(v_{\parallel}^2 + \mu - \frac{3}{2}\right)\omega_T\right] F_0 ik_y \chi_j - \sqrt{2}v_{\parallel} ik_z g_j - \sqrt{2}v_{\parallel} q_j F_0 ik_z \chi_j \ . \qquad (1)$$

Here, ω_{c} is the complex mode frequency in units of v_{th}/L_z with negative (positive) sign of the real part ω denoting electron (positron) frequencies; g_j is the perturbed modified distribution function, relating to its unmodified counterpart via $g_j = f_j + \sqrt{2}q_j v_{\parallel} J_0(\lambda_j) A_{\parallel} F_0$; moreover, $k_{x,y,z}$ refer to the wavenumbers in the x (along $\omega_{n,T}$), y (perpendicular to x and z), and z directions, normalized as $k_{x,y}\rho_{\text{e}}$ and $k_z L_z$, suggesting $k_z \ll k_{x,y}$ in physical units. The

generalized potential reads

$$\chi_j = J_0(\lambda_j)\Phi - \sqrt{2}v_\parallel J_0(\lambda_j)A_\parallel + \frac{2}{q_j}\frac{J_1(\lambda_j)}{\lambda_j}\mu B_\parallel = J_0\Phi - \sqrt{2}v_\parallel J_0 A_\parallel + \frac{2}{q_j}\bar{J}_1\mu B_\parallel \;, \quad (2)$$

where $J_{0,1}$ denote Bessel functions of argument $\lambda_j = q_j k_\perp (2\mu)^{1/2}$, with $k_\perp = (k_x^2 + k_y^2)^{1/2}$. As $J_0 = J_0(\lambda_j)$ is an even function, it has no species dependence due to $q_j = \pm 1$, and one may eliminate said dependence for the other Bessel function by defining $\bar{J}_1 \equiv J_1(\lambda_j)/\lambda_j$.

The field equations can be written as

$$\Phi = \left(k_\perp^2 \lambda_D^2 + 2(1 - \Gamma_0)\right)^{-1} \pi \int J_0(g_p - g_e) dv_\parallel d\mu \;, \quad (3)$$

$$B_\parallel = \left(-\frac{2}{\beta} - 4(\Gamma_0 - \Gamma_1)\right)^{-1} 2\pi \int \bar{J}_1(g_p + g_e)\mu dv_\parallel d\mu \;, \quad (4)$$

and

$$A_\parallel = \left(k_\perp^2 + \beta\Gamma_0\right)^{-1} \frac{\pi\beta}{\sqrt{2}} \int J_0(g_p - g_e)v_\parallel dv_\parallel d\mu \;. \quad (5)$$

In addition to the Debye length λ_D in units of ρ_e, the quantities $\Gamma_{0,1} \equiv \exp(-k_\perp^2)I_{0,1}(k_\perp^2)$ with the Bessel functions $I_{0,1}$ have been introduced in these equations.

Inserting the Vlasov equation into the field equations and defining $\alpha \equiv -\omega_c/(\sqrt{2}k_z)$, one obtains three coupled equations containing integrals of the form

$$\int_{-\infty}^{\infty} \frac{v_\parallel^a e^{-v_\parallel^2}}{v_\parallel - \alpha} dv_\parallel \quad \text{and} \quad \int_0^{\infty} e^{-\mu}\mu^a J_0^b \bar{J}_1^c d\mu \;,$$

(with a, b, and c denoting positive or zero integer numbers) where the former can be solved through rewriting in terms of the plasma dispersion function and using a large-argument expansion

$$Z(\alpha) \equiv \frac{1}{\sqrt{\pi}}\int_{-\infty}^{\infty} \frac{e^{-v_\parallel^2}}{v_\parallel - \alpha} dv_\parallel \approx -\alpha^{-1} - \alpha^{-3}/2 - 3\alpha^{-5}/4 \;. \quad (6)$$

This requires that the mode of interest be purely growing ($\omega = 0$) at a rate γ much larger than the parallel wavenumber k_z, a condition fully justifiable for the parameter cases studied here based on direct simulations. In addition, the Z function expansion is only required for the case of $k_z \neq 0$. The μ integrals can be solved exactly, producing different combinations of Γ_0 and Γ_1. Further defining $\Omega_1 \equiv (\Gamma_0 - \Gamma_1)\omega_n - [2k_\perp^2(\Gamma_0 - \Gamma_1) - \Gamma_0]\omega_T$ and $\Omega_2 \equiv (\Gamma_0 - \Gamma_1)\omega_n - [2k_\perp^2(\Gamma_0 - \Gamma_1) - 2\Gamma_0 + \Gamma_1]\omega_T$, the set of coupled field equations becomes

$$\left(k_\perp^2 \lambda_D^2 + 2(1 - \Gamma_0)\right)\Phi = -\frac{2k_y}{\omega_c}\Omega_1 B_\parallel + \frac{2k_z^2}{\omega_c^2}\Gamma_0\Phi + \frac{2k_z}{\omega_c}\Gamma_0 A_\parallel \;, \quad (7)$$

10

$$\left(-\frac{2}{\beta} - 4(\Gamma_0 - \Gamma_1)\right) B_\parallel = -\frac{2k_y}{\omega_c}\Omega_1\Phi - \frac{2k_yk_z}{\omega_c^2}\Omega_2 A_\parallel + \frac{4k_z^2}{\omega_c^2}(\Gamma_0 - \Gamma_1)B_\parallel \,, \tag{8}$$

and

$$\left(k_\perp^2 + \beta\Gamma_0\right) A_\parallel = \frac{\beta k_yk_z}{\omega_c^2}\Omega_2 B_\parallel - \frac{\beta k_z}{\omega_c}\Gamma_0\Phi - \frac{3\beta k_z^2}{\omega_c^2}\Gamma_0 A_\parallel \,. \tag{9}$$

Solving this set produces a quartic equation for ω_c^2,

$$\begin{aligned}
&\left\{ 4k_y^2\Omega_1^2\omega_c^2 + 4k_z^2(\Gamma_0 - \Gamma_1)\left[\left(k_\perp^2\lambda_D^2 + 2 - 2\Gamma_0\right)\omega_c^2 - 2k_z^2\Gamma_0\right] \right. \tag{10} \\
&\left. + \left(\frac{2}{\beta} + 4\Gamma_0 - 4\Gamma_1\right)\left[\left(k_\perp^2\lambda_D^2 + 2 - 2\Gamma_0\right)\omega_c^4 - 2k_z^2\Gamma_0\omega_c^2\right]\right\} \\
&\cdot \left\{ k_\perp^2\left[\omega_c^4\left(k_\perp^2\lambda_D^2 + 2 - 2\Gamma_0\right) - \omega_c^2 2k_z^2\Gamma_0\right] + \beta\Gamma_0\left[\omega_c^4\left(k_\perp^2\lambda_D^2 + 2 - 2\Gamma_0\right) - \omega_c^2 2k_z^2\Gamma_0\right] \right. \\
&\left. + \omega_c^2 2\beta k_z^2\Gamma_0^2 + 3\beta k_z^2\Gamma_0\left[\omega_c^2\left(k_\perp^2\lambda_D^2 + 2 - 2\Gamma_0\right) - 2k_z^2\Gamma_0\right]\right\} \\
&= \left\{ \omega_c^2\Omega_1 4k_yk_z\Gamma_0 + \Omega_2 2k_yk_z\left[\omega_c^2\left(k_\perp^2\lambda_D^2 + 2 - 2\Gamma_0\right) - 2k_z^2\Gamma_0\right]\right\} \\
&\cdot \left\{ \beta k_yk_z\Omega_2\left[\omega_c^2\left(k_\perp^2\lambda_D^2 + 2 - 2\Gamma_0\right) - 2k_z^2\Gamma_0\right] + \omega_c^2\Omega_1 2\beta k_yk_z\Gamma_0\right\} \,,
\end{aligned}$$

which can be solved exactly. First, however, it is instructive to focus on the case of $k_z = 0$, for which the GDC growth rate becomes

$$\gamma = \frac{2k_y\Omega_1}{[(k_\perp^2\lambda_D^2 + 2 - 2\Gamma_0)(2/\beta + 4\Gamma_0 - 4\Gamma_1)]^{1/2}} \,. \tag{11}$$

For practical applications, perpendicular length scales are often much larger than the gyroradius, or $k_\perp \ll 1$, leading to

$$\gamma = \frac{\sqrt{2}k_y(\omega_n + \omega_T)}{k_\perp\sqrt{(2 + 1/\beta)(2 + \lambda_D^2)}} \,. \tag{12}$$

This expression provides a transparent exposition of essential physics: the GDC is destabilized equally by density and temperature gradients, scales as $\beta^{1/2}$ due to $B_\parallel$, one of the two contributing fields, being proportional to β, and is stabilized by the Debye length.

Figure 3 illustrates the validity of Eq. (12) for independent parameter variations in β, λ_D, k_x, and $\omega_{n,T}$: it shows the predicted growth rates (solid lines) to be in excellent agreement with the individual data points from gyrokinetic simulations using the full linear operator for the unsheared slab, assuming no force balance. Simulations were performed with the GENE code [32, 33], with up to 128 parallel, 32 parallel velocity, and 8 magnetic moment grid points. At $k_z = 0$, the full linear eigenvalue system was solved, returning the unstable
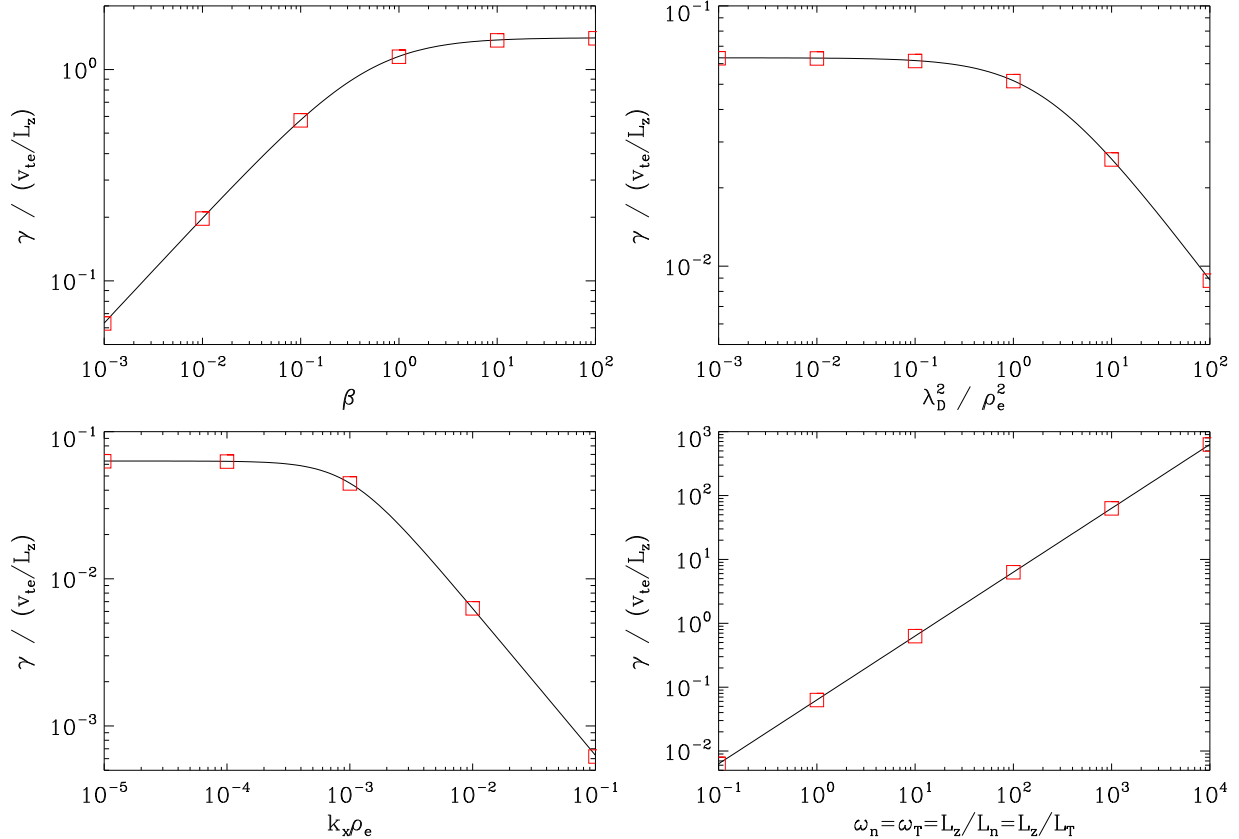
FIG. 3. Parametric dependencies of the dominant $k_z = 0$ GDC instability for scans of the normalized pressure β, the Debye length λ_{D}, the wavenumber k_x, and the driving gradients $\omega_{n,T}$. Black solid lines represent the solution given in Eq. (12), while red squares denote gyrokinetic simulation results; good agreement is observed throughout these scans—at even higher k_x, however, the low-$k_\perp$ approximation will break down.

and stable GDC branches at $\pm|\gamma|$ in addition to a large number of marginally stable modes at $\gamma \approx 0$. The base physical parameter set reads $\beta = 0.001$, $\lambda_{\mathrm{D}} = 0.01$, $k_x = 0$, $k_z = 0$, $\omega_n = \omega_T = 1$ at $k_y = 0.001$.

One of the advantages of using the gyrokinetic approach over the fully kinetic simulations in Sec. II is that the linear operator can be inverted, allowing the extraction of growth rates to machine precision without pollution by noise from initial conditions or other effects.

The picture becomes more complex once finite k_z are taken into consideration. As Fig. 4 shows, γ is reduced with increasing k_z, a finding which is expected to hold for ion-electron plasmas, as well [26]. While direct simulation and the fastest-growing solution of Eq. (10) agree well for these parameters ($\beta = 0.01$, $\lambda_{\mathrm{D}} = 0$, $k_x = 0$, $\omega_n = \omega_T = 500$ at $k_y = 0.1$), the
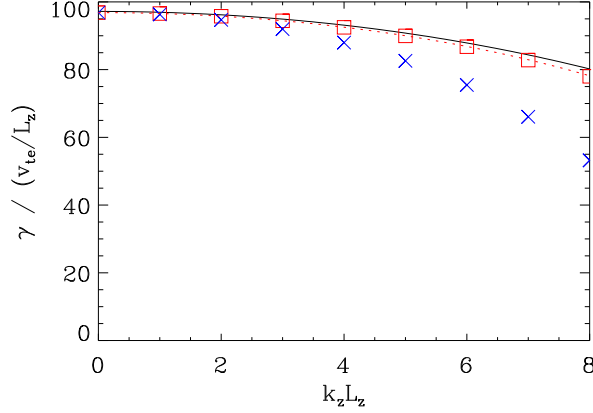
FIG. 4. GDC growth rates vs. parallel wavenumber k_z, showing the stabilizing effect of parallel dynamics. The black solid line represents the solution to the dispersion relation Eq. (10), red squares are gyrokinetic simulations, and the red dotted line is a fit to the corresponding simulation data points, see the text. Also shown as blue crosses are gyrokinetic simulations where $A_\parallel$ was artificially removed.

existence and dependencies of other growing roots in conjunction with the large-argument expansion of the plasma dispersion function make it necessary to pay close attention to ordering when considering other regions of parameter space.

Also included in the figure is a fit (red dotted line) to the simulation data. For the present parameters, one may reduce Eq. (10) to a quadratic equation in ω_c^2, and further ordering considerations allow for the growth rate to be written as $\gamma^2 \approx a - bk_z^2$. Clearly, the simulations are obeying this relation.

To isolate the impact of $A_\parallel$ fluctuations at finite k_z, results from simulations artificially setting $A_\parallel = 0$ are shown as blue crosses in Fig. 4, demonstrating that unlike for the $k_z = 0$ case, $A_\parallel$ now couples into the GDC via a $\nabla B_\perp$ drift, adding another drift-coupling level. This aspect may be at least partially responsible for the $A_\parallel$ signatures seen in the helium plasma simulations of Ref. [26].

A physical picture of the finite-k_z GDC modifications emerges. For the small-β limit, the primary effect results from the neutrally stable electrostatic drift wave now enabled in Eq. (7). Another, similar compressional magnetic wave can be ignored due to $\Phi \gg B_\parallel$. The electrostatic wave effectively reduces the amplitude of Φ available to the GDC mechanism, resulting in partial stabilization. By adding $A_\parallel$ into the picture, the Φ term in Eq. (9) –
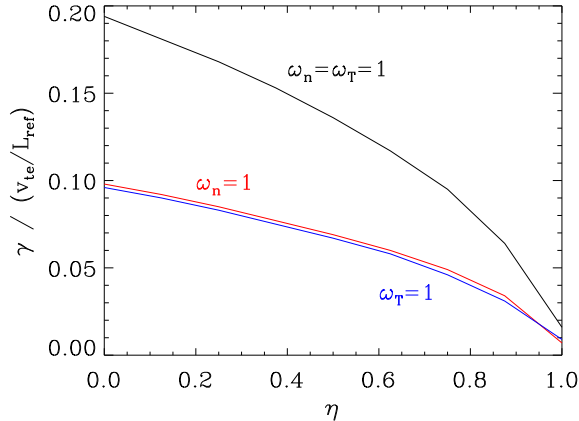
13

FIG. 5. GDC growth rates as functions of force-balance scaling parameter η. Shown are cases of equal density and temperature gradients (black), only a density gradient (red), and only a temperature gradient (blue). In all cases, the mode becomes marginal as force balance is achieved at $\eta = 1$.

corresponding to current density produced by charges scattered by electric field fluctuations – governs shear-magnetic fluctuations; using it to replace $A_\parallel$ in Eq. (7), it reduces the electrostatic wave amplitude, mitigating its stabilizing effect on the GDC. For the above choice of $k_\perp^2 = \beta$, the relative strengths of these Φ and $A_\parallel$ effects differ by a factor of two, clearly in agreement with the red squares and blue crosses in Fig. 4.

Note that the subdominant finite-k_z GDC, as opposed to the dominant $k_z = 0$ branch, is only likely to play a role in cases where large normalized gradients occur, such that immediate stabilization of the GDC at even the lowest k_z in the system does not occur. One such example is given in Ref. [26], where the second parallel harmonic of the GDC was seen to be unstable.

Given the findings of Sec. II, it is instructive to determine how the equilibrium magnetic field may affect the mode. Figure 5 shows linear GDC growth rates for different gradient settings, as the force balance condition is continuously adjusted via a scaling factor η in $\omega_B = -\eta\beta(\omega_n + \omega_T)$, such that force balance is fully achieved at $\eta = 1$. Consistent with the results reported in Ref. [28], the instability vanishes as $\eta \to 1$, with small finite γ values resulting from finite numerical resolution. Importantly, the data also suggests that even a modest amount of continuous forcing away from diamagnetic equilibrium is sufficient to allow maintaining a GDC-unstable state.
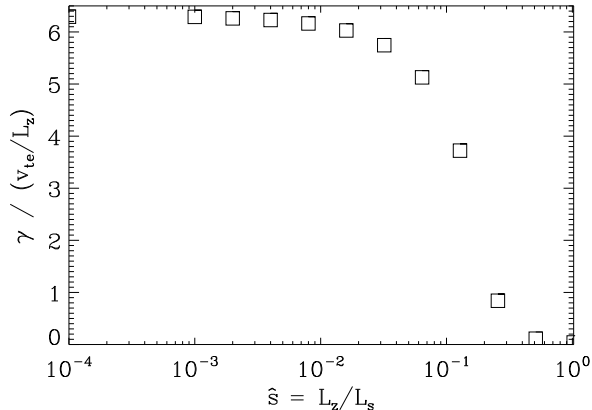
14

FIG. 6. Stabilizing impact of background magnetic shear $\hat{s}$ on the growth rate. For the present choice of $\omega_n = \omega_T = 100$, the normalized shear required for full stabilization is much smaller than the driving gradients.

Returning to the case of $\eta = 0$, the impact of background magnetic shear is studied. The growth rate scaling seen in Fig. 6 with the normalized shear $\hat{s} = L_z/L_s$ confirms the strongly stabilizing effect of $\hat{s}$; these simulations were performed at $\beta = 0.001$ and $\omega_n = \omega_T = 100$, in the low-$k_\perp$ limit of $k_y = 10^{-3}$ and $k_x = 0$ (note that higher k_x are included in the simulation due to a twist-and-shift parallel boundary condition). Clearly, only very moderate shear is required to fully suppress GDC growth, suggesting that this instability may only exist in unsheared systems. However, note that a possible path to mode excitation in sheared geometry exists for higher wavenumbers [34].

Having obtained a more thorough understanding of the underlying GDC physics, the next step is to design a reduced model capturing the most pertinent effects.

IV. REDUCED FLUID MODEL

One of the shortcomings of the analysis in Ref. [26] is that in a radially periodic local flux tube, the GDC will invariably develop at radial system size, necessitating restrictive assumptions to avoid unphysical boundary effects. While a global gyrokinetic framework with $B_\parallel$ fluctuations is presently under development [35], it is possible to tackle the radially global case with a fluid model based on the drift-kinetic equations, thus circumventing the complexities of treating the Larmor-radius-scale physics.

As a starting point, a simple local fluid model is formulated, containing the mechanisms

15

for GDC in pair plasmas. Again assuming identical temperature and density profiles of the species j, ignoring parallel dynamics (and thus $A_\parallel$ fluctuations), and focusing on the drift-kinetic limit of $k_\perp \ll 1$, the nonlinear normalized gyrokinetic equations read

$$\partial_t f_j = -\left[\omega_n + \left(v_\parallel^2 + \mu - \frac{3}{2}\right)\omega_T\right]F_0 ik_y\chi_j + \sum_{k'}\left(k_x'k_y - k_xk_y'\right)\chi_j(k')f_j(k - k') , \quad (13)$$

$$\Phi = \frac{\pi}{k_\perp^2(2 + \lambda_D^2)}\int(f_p - f_e)\mathrm{d}v_\parallel\mathrm{d}\mu , \quad (14)$$

$$B_\parallel = \frac{\pi}{-2/\beta - 4}\int\mu(f_p + f_e)\mathrm{d}v_\parallel\mathrm{d}\mu , \quad (15)$$

with $\chi_j = \Phi + \mu B_\parallel/q_j$. Using the respective definitions for density and temperature fluctuations,

$$n_j = \pi\int f_j\mathrm{d}v_\parallel\mathrm{d}\mu \quad (16)$$

and

$$T_{\perp j} = \pi\int(\mu - 1)f_j\mathrm{d}v_\parallel\mathrm{d}\mu , \quad (17)$$

one can compose the following four-field model by integrating Eq. (13) over velocity space, with and without weight μ:

$$\partial_t n_j = -ik_y\left[\omega_n\Phi + \frac{1}{q_j}(\omega_n + \omega_T)B_\parallel\right] \quad (18)$$
$$+ \sum_{k'}\left(k_x'k_y - k_xk_y'\right)\left[\Phi(k')n_j(k - k') + \frac{1}{q_j}B_\parallel(k')\left(T_{\perp j}(k - k') + n_j(k - k')\right)\right] ,$$

$$\partial_t T_{\perp j} = -ik_y\left[\omega_T\Phi + \frac{1}{q_j}(\omega_n + 3\omega_T)B_\parallel\right] \quad (19)$$
$$+ \sum_{k'}\left(k_x'k_y - k_xk_y'\right)\left[\Phi(k')T_{\perp j}(k - k') + \frac{1}{q_j}B_\parallel(k')\left(\int(\mu^2 - \mu)f_j(k - k')\mathrm{d}^3v\right)\right] ,$$

$$\Phi = \frac{n_p - n_e}{k_\perp^2(2 + \lambda_D^2)} , \quad (20)$$

$$B_\parallel = \frac{T_{\perp p} + T_{\perp e} + n_p + n_e}{-2/\beta - 4} . \quad (21)$$

Notably, the nonlinearity of the second equation of this set still contains a velocity-space integral. A more thorough analytical and numerical treatment will be necessary to obtain proper closure characteristics; simply dropping the term or integrating it under the assumption of a Maxwellian velocity space leads to numerical instability – even at drastically reduced time steps – and rapid growth without bound at a rate orders of magnitude greater than the linear growth rate.
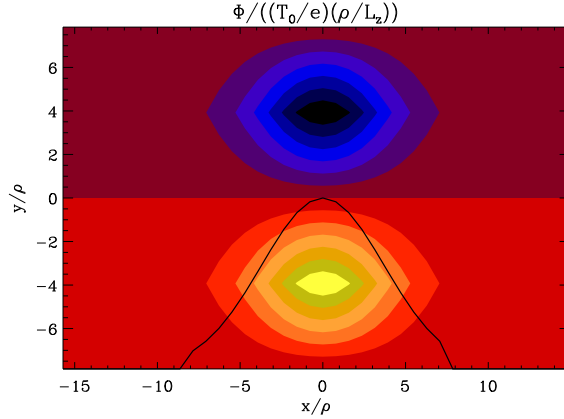
16

$$\Phi/((T_0/e)(\rho/L_z))$$

FIG. 7. Φ contours of the global GDC eigenfunction as evaluated by the fluid model; $B_\parallel$, not shown here, has a similar structure but is phase-shifted by π along y. The black line in the lower half of the plot symbolizes the profile of $\omega_n(x)$, falling off to zero towards the ends of the box and peaking at a value of one at the center. Colors represent mode amplitude Φ in arbitrary units.

Linearizing these equations, one may straightforwardly recover the correct driftkinetic linear growth rate in Eq. (12). Had one not retained $T_{\perp j}$ fluctuations and built a model based on n_j alone, the correct instability physics would not have emerged.

A simple global version of the linearized version of these equations is obtained by transforming to real space in x, adding numerical diffusion, and imposing gradient profiles that fall off at the boundary. Aside from the nonlinearities dropping out, the only change to the equations is that now, all fields are functions of (x, k_y), that $\omega_n = L_z/L_n$ and $\omega_T = L_z/L_T$ contain the (arbitrary) x structure of the density and temperature gradient profiles, and that the k_x factors in $k_\perp$ are now replaced by ∂_x operators.

The result from evaluating this new set can be seen in Fig. 7, where the model is evaluated for the same physical parameters as those in Sec. II but for the density gradient profile indicated by the black line. The eigenfunction in the x-y plane, as indicated by the colors, stretches to the width of the gradient profile—a reduction in this width has a stabilizing impact on the growth rate, as is to be expected.

Overall, global simulations lead to the following conclusions. First, the width of the eigenmode along x is constrained only by the profile shape. Second, linear growth rates match gyrokinetic flux-tube results for sufficiently large box sizes in the appropriate $k_\perp \ll 1$ limit.

17

While additional work will be necessary for a better understanding of saturation and nonlinear dynamics, this framework can be used to benchmark linear global gyrokinetics.

V. APPLICATION TO PHYSICAL SYSTEMS

Having derived a general growth rate expression for the dominant $k_z = 0$ GDC and having verified the same against direct simulations in Sec. III, one may estimate the impact of GDC growth on various physical systems. Growth rates are primarily set by values of β and the Debye length (in units of the gyroradius)—see also Ref. [36]. Note that the following applications are inherently exploratory, and more sophisticated, extensive modeling will be necessary for true quantitative predictions.

While its unsheared but curved magnetic fields require additional study, one may investigate the limits relevant to the APEX experiment, which are large λ_D and small β. For estimated APEX parameters least conducive to GDC growth, $\lambda_D \sim 1000$ and $\beta \sim 10^{-10}$, and assuming $\omega_n = L_z/L_n = \omega_T = L_z/L_T$, the growth rate is given by $\gamma = (8\beta)^{1/2}/\lambda_D = 2.8{\times}10^{-8}$ in units of v_{th}/L_n. Focusing on different regions in the dipole field, changes in $\beta \sim 10^{-9}$ and $\lambda_D \sim 30$ lead to much faster growth at $\gamma = 3.0\times10^{-6}$. Thus, a characteristic GDC growth time in APEX may be on the order of $0.01 - 1\,\mathrm{s}$, which could be detectable given projected plasma lifetimes of up to a few seconds. Note that this presumes that pair injection is sufficiently fast that pressure gradients are fully established before the magnetic field can react. Extending the present work to an unsheared dipole field will enable more quantitative predictions of GDC turbulence in this device.

Before venturing into the two subsequent, relativistic applications, it is both appropriate and necessary to offer a brief discussion of the physics at high velocities approaching the speed of light c. The scope of this work precludes a fully special-relativistic treatment; while publications on relativistic gyrokinetics exist [37–39], they cover only the initial stages of the derivations required to arrive at the equations on which the present work is based. Regardless, certain considerations allow an assessment of the impact of relativistic energies on the physics at hand. Cases where thermal velocities in the rest frame of the plasma are $v_{th} \lesssim 0.1c$ can be treated non-relativistically, and results merely have to be modified by a bulk Lorentz factor Γ. Situations with relativistic $v_{th} > 0.1c$ are more difficult to assess—however, work on other instabilities (see, e.g., Ref. [40]) suggests that growth rates mostly

scale no more strongly than linearly in Γ. For the examples studied below, this implies corrections of order $\mathcal{O}(1)$. As the present work merely aims to assess via order-of-magnitude estimates whether GDC growth may be relevant, no relativistic corrections are included here, deferring such model improvements to future work.

Reference [16] describes the creation of an electron-positron plasma by means of a target interaction by a laser-induced electron beam. This experimental scenario similarly lends itself to the GDC – implicitly providing a possible test of GDC activity in weakly magnetized plasmas – with the appropriate limits of $\lambda_D \ll 1$ and $\beta \gg 1$ reducing Eq. (12) to $\gamma = (\omega_n + \omega_T)/\sqrt{2}$. It is to be noted, however, that for these β values, $A_\parallel$ can couple to the $B_\parallel$-Φ system even at $k_z = 0$, making high-precision quantitative predictions more difficult.

In the rest frame, the electron-positron plasma on its flight path has a temperature of $T_0 \sim 3 \times 10^7$ eV (and thus v_{th} at approximately the speed of light) and gradient length scales on the order of $100\,\mu$m, resulting in a GDC growth time of about 10^{-13} s in the co-moving frame. Even at a bulk Lorentz factor of $\mathcal{O}(10)$, GDC growth occurs at a rate much faster than the time-of-flight of about 10^{-9} s, implying the possibility of measuring the GDC-prompted growth of fluctuations along the flight path. While quantitative predictions will require nonlinear simulations, this discrepancy in time scales, along with a sufficiently large initial perturbation level, suggests that fluctuations – either in the linear or in a nonlinear phase – would be observable. At the end of the flight path, Ref. [16] shows beam cross-sections of the electron and positron densities. By performing equivalent measurements at the beginning of the flight path, the change in fluctuation amplitude can be quantified and related to the above GDC prediction, taking into account beam divergence [41]. Experimentally, this test will require the addition of a magnetic field for the flight path—a field strength of 1 T would lead to marginal magnetization (i.e., gyroradii of system size), with larger fields or larger plasma volumes providing safer routes to GDC validation. Given the non-equilibrium nature of such experiments, force balance does not become a consideration here.

As a third application, GRBs offer a greater challenge, as different GRB phases – sometimes associated with competing physical models – can correspond to vastly different parameter regimes. Thermal velocities lie between 0.1 and 1 in units of the speed of light, and gradient scale lengths may range from 10^6 to 10^{18} cm. Using the aforementioned limit of large β and small λ_D, GDC growth times span the enormous range of 10^{-5} to 10^8 s. Future investigation focusing on specific GRB phases – such as the collision of expanding electron-

positron shells – will have to reveal when GDC growth may be occurring for sufficiently long periods to imprint fluctuation signals. If this should indeed be the case, the tendency of finite-k_z GDC to couple into $A_\parallel$ may add another layer of complexity to the Weibel-based synchrotron radiation process.

Also note that newer models of GRB outflows rely on baryonic winds [42], where the evaluation of GDC growth rates or the subsequent formation of turbulent fluctuations would require direct numerical evaluation, which are left for future investigation.

VI.   CONCLUSIONS

By means of full-f kinetic simulations, it has been demonstrated that GDC instability and turbulence can be excited when a Maxwellian pair plasma with a pressure inhomogeneity is placed in a homogeneous magnetic guide field. In the scenarios investigated here, where $\omega_n/\omega_T > 0$, the GDC mode is the only instability driven by a density or temperature gradient. Force balance will ultimately be achieved by a combination of flattening of the pressure gradient due to GDC-turbulence-induced transport and the formation of a magnetic field gradient. In a fully force-balanced equilibrium, the GDC growth rate becomes zero.

For cases with strong magnetization, gyrokinetic theory and simulations capture all relevant GDC physics. In particular, the linear growth rate for the dominant $k_z = 0$ mode branch in the absence of force balance can be evaluated as

$$\gamma = \frac{\sqrt{2}k_y(\omega_n + \omega_T)}{k_\perp \sqrt{(2 + 1/\beta)(2 + \lambda_{\mathrm{D}}^2)}}$$

for small perpendicular wavenumbers. When resolving finite-k_z physics, the fields Φ and $B_\parallel$ additionally couple to shear-magnetic fluctuations $A_\parallel$, causing partial stabilization of the GDC; similarly, the instability only exists when the background magnetic shear is small. Based on these considerations, a reduced fluid model has been derived which reproduces gyrokinetic predictions in the appropriate limits and which can be deployed in cases with radially varying gradient scale lengths.

Applying these findings to terrestrial electron-positron experiments yields potentially dynamically relevant growth times. For the APEX device, this requires turbulence to develop during and soon after plasma injection, as at later times force balance will suppress the instability drive. In the case of laser-induced plasma studies, such as those reported in

Refs. [13, 16], force balance is of no concern; here, a mechanism for identifying GDC activity is suggested via spatial beam characterization at different positions along the flight path. When considering naturally occurring electron-positron plasmas in gamma-ray bursts, growth times cover a wide range, from a millisecond to a multi-year timescale, necessitating further work to determine the potential impact of the GDC and possible observation characteristics.

One next step will be to assess how GDC instability imprints turbulence simulations of the systems investigated above. The resulting predicted fluctuation signatures can then be validated against observation data.

---

[1] T.H. Stix, *Waves in Plasmas*, AIP-Press (1992)

[2] S. Chandrasekhar, *Hydrodynamic and Hydromagnetic Stability*, New York: Dover (1961)

[3] H. Alfvén, Astrophys. J. **133**, 1049 (1961)

[4] A.N. Kolmogorov, Dokl. Akad. Nauk SSSR **30**, 299 (1941)

[5] B. Coppi, Phys. Lett. **11**, 226 (1964)

[6] W. Horton, Rev. Mod. Phys. **71**, 735 (1999)

[7] H.P. Furth, J. Killeen, and M.N. Rosenbluth, Phys. Fluids **6**, 459 (1963)

[8] S. Chandrasekhar, A.N. Kaufman, and K.M. Watson, Proc. Roy. Soc. London, Ser. A **245**, 435 (1958)

[9] E.S. Weibel, Phys. Rev. Lett. **2**, 83 (1959)

[10] M.J. Rees, Nucl. Phys. A **663**, 42c (2000)

[11] G. Gabrielse, A. Khabbaz, D.S. Hall, C. Heimann, H. Kalinowsky, and W. Jhe, Phys. Rev. Lett. **82**, 3198 (1999)

[12] G. Sarri, M.E. Dieckmann, I. Kourakis, A. Di Piazza, B. Reville, C.H. Keitel, and M. Zepf,

J. Plasma Phys. **81**, 455810401 (2015)

[13] M. Lobet, C. Ruyer, A. Debayle, E. d'Humières, M. Grech, M. Lemoine, and L. Gremillet, Phys. Rev. Lett. **115**, 215003 (2015)

[14] H. Chen, J. Bonlie, R. Cauble, F. Fiuza, W. Goldstein, A. Hazi, C. Keane, A. Link, E. Marley, S.R. Nagel, *et al.*, J. Phys. Conf. Ser. **688**, 012010 (2016)

[15] M. Lobet, X. Davoine, E. d'Humières, and L. Gremillet, Phys. Rev. Accel. Beams **20**, 043401 (2017)

[16] G. Sarri, K. Poder, J.M. Cole, W. Schumaker, A. Di Piazza, B. Reville, T. Dzelzainis, D. Doria, L.A. Gizzi, G. Grittani, *et al.*, Nat. Commun. **6**, 6747 (2015)

[17] P. Helander, Phys. Rev. Lett. **113**, 135003 (2014)

[18] P. Helander and J.W. Connor, J. Plasma Phys. **82**, 905820301 (2016)

[19] H. Saitoh, T.S. Pedersen, U. Hergenhahn, E.V. Stenson, N. Paschkowski, and C. Hugenschmidt, J. Phys. Conf. Ser. **505**, 012045 (2014)

[20] E.V. Stenson, H. Saitoh, J. Stanja, H. Niemann, U. Hergenhahn, T. Sunn Pedersen, G.H. Marx, L. Schweikhard, J.R. Danielson, C.M. Surko, and C. Hugenschmidt, AIP Conf. Proc. **1668**, 040004 (2015)

[21] A. Mishchenko, G.G. Plunk, and P. Helander, J. Plasma Phys. **84**, 905840201 (2018)

[22] T. Sunn Pedersen, A.H. Boozer, W. Dorland, J.P. Kremer, and R. Schmitt, J. Phys. B **36** 1029 (2003)

[23] M.J. Pueschel, F. Jenko, D. Told, and J. Büchner, Phys. Plasmas **18**, 112102 (2011)

[24] M.J. Pueschel, P.W. Terry, D. Told, and F. Jenko, Phys. Plasmas **22**, 062105 (2015)

[25] M.J. Pueschel, D. Told, P.W. Terry, F. Jenko, E.G. Zweibel, V. Zhdankin, and H. Lesch, Astrophys. J. Suppl. Ser. **213**, 30 (2014)

[26] M.J. Pueschel, G. Rossi, D. Told, P.W. Terry, F. Jenko, and T.A. Carter, Plasma Phys. Control. Fusion **59**, 024006 (2017)

[27] R.D. Sydora, J. Comp. Appl. Math. **109**, 243 (1999)

[28] B.N. Rogers, B. Zhu, and M. Francisqez, Phys. Plasmas **25**, 052115 (2018)

[29] D.R. Hatch, F. Jenko, A. Bañón Navarro, V. Bratanov, P.W. Terry, and M.J. Pueschel, New J. Phys. **18**, 075018 (2016)

[30] K.D. Makwana, P.W. Terry, J.-H. Kim, and D.R. Hatch, Phys. Plasmas **18**, 012302 (2011)

[31] A.J. Brizard and T.S. Hahm, Rev. Mod. Phys. **79**, 421 (2007)

[32] F. Jenko, W. Dorland, M. Kotschenreuther, and B.N. Rogers, Phys. Plasmas **7**, 1904 (2000)

[33] see http://www.genecode.org for code details and access

[34] M. Landreman, T.M. Antonsen, and William Dorland, Phys. Rev. Lett. **114**, 095003 (2015)

[35] S.-W. Tsao, M.J. Pueschel, and D.R. Hatch, Proceedings of the 61st Annual Meeting of the APS Division of Plasma Physics (American Physical Society, New York, 2019)

[36] E.V. Stenson, J. Horn-Stanja, M.R. Stoneking, and T. Sunn Pedersen, J. Plasma Phys. **83**, 595830106 (2017)

[37] R.G. Littlejohn, Phys. Fluids **27**, 976 (1984)

[38] A.J. Brizard and A.A. Chan, Phys. Plasmas **6**, 4548 (1999)

[39] A. Beklemishev and M. Tessarotto, Astron. Astrophys. **428**, 1 (2004)

[40] M. Lemoine and G. Pelletier, Mon. Not. R. Astron. Soc. **402**, 321 (2010)

[41] G. Sarri, J. Warwick, W. Schumaker, K. Poder, J. Cole, D. Doria, T. Dzelzainis, K. Krushelnick, S. Kuschel, S.P.D. Mangles, *et al.*, Plasma Phys. Control. Fusion **59**, 014015 (2017)

[42] D. Lazzati, R. Ciolfi, and R. Perna, Astrophys. J. **898**, 59 (2020)